Atmospheric Research 285 (2023) 106657

Contents lists available at ScienceDirect

Atmospheric Research

journal homepage: www.elsevier.com/locate/atmosres

Assessment of cloudless-to-cloud transition zone from downwelling longwave irradiance measurements

Josep-Abel González [a,*], Josep Calbó [a], Yolanda Sola [b]

[a] Grup de Física Ambiental, Departament de Física, Universitat de Girona, Catalonia, Spain
[b] Grup de Meteorologia, Departament de Física Aplicada, Universitat de Barcelona, Catalonia, Spain

ARTICLE INFO

Keywords:
Cloud-aerosol transition zone
Twilight zone
Cloud detection
Clear sky detection
Longwave irradiance

ABSTRACT

The transition zone has been defined as corresponding to atmospheric conditions between cloud-free (albeit containing a suspension of dry particles, i.e. aerosol) and clouds (air containing a suspension of highly hydrated particles, i.e. droplets or ice crystals). Since clouds significantly affect the infrared radiation reaching the Earth's surface, broadband infrared measurements, which are usually performed with pyrgeometers, are implicated in some of the methods proposed for detecting clouds. The present work uses one of these methods to characterize the transition between cloud-free and cloudy conditions. Two years of downwelling longwave irradiance measured with a pyrgeometer located in Girona (in the northeast of the Iberian Peninsula) have been used to determine the values of a cloud detection index. The method must be previously tuned against a set of selected cloud-free cases to detect cloudiness to a certain confidence level. The effect of changing the detection confidence level was studied and used to derive the occurrence of transition conditions. The performance of the cloudiness detection method, with the support of observations by broadband shortwave instruments, ceilometer retrievals and images captured by hemispherical camera, was then analyzed for some short time periods. The duration of the transition periods is presented here, showing that 41% are very short (10 min, the temporal resolution of the detection method), that the median of the distribution is about 20 min, and that, although periods of more than one hour are observed, longer durations steadily decrease in frequency. It was found that 10–15% of the observations included may correspond to the transition zone, thus strengthening the estimations from other shortwave-based methods that are only suitable for daylight periods.

1. Introduction

Aggregates of particles suspended in air are classified as cloud or aerosol in relation to the water content of the particles: cloud particles can be considered an extreme condition in which non-aqueous particles (aerosol), acting as condensation nuclei, become highly hydrated. Several properties have been considered to distinguish between the two states and to characterize them: particle composition, mainly proportion of water content, size distribution as the particles grow when hydrated, and radiative effects in various spectral bands, including the appearance in the visible range of human observers. The dynamics and the evolution of the aggregates can further help to distinguish their nature. However, to the extent that cloud and atmospheric aerosol can be envisioned as different regimes of the same phenomenon, a continuum of intermediate conditions between cloud and cloud-free air (i.e., containing only suspended particles qualified as aerosol) should be considered when dealing with remote sensing of the atmosphere and radiative and atmospheric modeling. This intermediate region has been described in the literature as a continuum of radiative properties (Charlson et al., 2007), a "twilight zone" (Koren et al., 2007), a "transition zone" (Chiu et al., 2009; Hirsch et al., 2014; Calbó et al., 2017a), or as some area showing cloud-adjacent effects (Várnai and Marshak, 2009; Chiu et al., 2009; Yang et al., 2016), and is receiving increasing attention. For example, several works deal with the radiative effect of suspensions of particles in the transition zone (Jahani et al., 2019; Jahani et al., 2020; Eytan et al., 2020; Jahani et al., 2022). The terms "cloud halo" or "humidity enhancement" have also been used to denote the region near the cloud with increased relative humidity (Perry and Hobbs, 1996; Lu et al., 2003; Koren et al., 2007; Yang et al., 2016). Likewise, the macroscopic geometric extent of clouds (Koren et al., 2008) or the scales at which cloudiness is detected from space (Di Girolamo and Davies, 1997), the frequency in the occurrence of transition regions (Schwarz et al., 2017),

* Corresponding author.
E-mail address: jose.gonzalez@udg.edu (J.-A. González).

https://doi.org/10.1016/j.atmosres.2023.106657
Received 9 October 2022; Received in revised form 2 February 2023; Accepted 6 February 2023
Available online 9 February 2023

the time scales at which their presence is detectable (Koren et al., 2007), and their very short scale (centimeter) optical properties (Schwartz et al., 2017) are becoming subjects of discussion. Even what can be considered a cloud is under discussion (see, for example, Di Girolamo and Davies, 1997, and the recent work of Spänkuch et al., 2022).

The assessment of the spatial extent and frequency of appearance of the transition zone is important because, as the radiative properties of clouds and aerosol (or cloud-free sky) are different and affect the energy balance in the climate system in different ways, they can lead to different large-scale radiative fluxes. Koren et al. (2007) estimated that, for an average global cloud fraction of 51%, a border area of 10 km (30 km) around cloud edges would lead to a transition zone reaching 17% (30%) of the global coverage, corresponding to 34% (60%) of the area considered cloud-free. According to Schwarz et al. (2017), 20% of all MODIS pixels were not well classified as cloud or aerosol, and were not accounted for radiative effects, for a set of observations over the analyzed periods (February and August 2007–2011). Moreover, Calbó et al. (2017a) estimated, for two locations (Girona, in the northeast of the Iberian Peninsula, and the Atmospheric Radiation Measurement program site in Boulder, CO), that about 10% of the time there is a suspension of particles in the air that is difficult to classify as cloud or aerosol.

In principle, any method of atmospheric sensing or radiative flux measurements can be used to detect macroscopic aggregates of suspended particles, namely clouds or aerosol. For this purpose, both passive and active methods may be suitable. Passive methods include those based on measurements employing broadband shortwave instruments (Long and Ackerman, 2000), spectral channel sunphotometers (CIMEL, Dubovik and King, 2000), multifilter rotating shadowband radiometers (MFRSR, Harrison et al., 1994), scanning spectroradiometers, and microwave radiometers. Whole sky imagers based on RGB cameras are also used to screen and characterize clouds and aerosol (see for example Long et al., 2006a, and more recent works by Kazantzidis et al., 2012, Letu et al., 2014, and Román et al., 2022). Moreover, neural network techniques are applied to characterize cloudiness from sky imagery (see for example the recent work of Fabel et al., 2022). Besides these, active devices such as radar and lidar (and ceilometers), and methods integrating different instruments (Active Remote Sensing of Clouds, ARSCL, Clothiaux et al., 2001) extend the techniques available for remote sensing of the atmosphere. Other techniques, such as radiosonde profiling (Costa-Surós et al., 2014), involve in-situ measurements. For a review of cloud detection and characterization methods, see Tapakis and Charalambides (2013).

In the abovementioned methods, instrumental detection or cloud screening to distinguish them from aerosol or cloud-free conditions requires (even for in-situ determination) the use of thresholds for some critical variables (or the tuning of some parameters) to be established beforehand, either on a theoretical or purely empirical basis. This affects any detection and characterization method that takes advantage of the radiative characteristics and effects of clouds, whether passive or active. Similarly, in meteorological modeling, some thresholds are involved to decide when/where a cloud would/should be present. The criteria used in the selection of thresholds, albeit reproducible, may introduce some subjectivity or arbitrariness, as human decisions do (Schwartz et al., 2017), which leads to some uncertainty in the cloudiness characterization and quantification. This uncertainty in satellite and ground-based cloud detection can have important consequences when assessing climatic effects. From a climate perspective, the globally averaged radiative forcing within transition areas of about 4 km around clouds is equivalent to adding 75 ppmv CO_2 to the atmospheric column (Eytan et al., 2020). Other studies have shown that avoiding near-cloud pixels, as they do not coincide with the thresholds for cloud and cloud-free conditions, results in a negative bias toward a drier atmosphere (Sohn et al., 2010).

The estimate of 10% of cases being difficult to classify as cloudy or cloud-free obtained by Calbó et al. (2017a) was based on uncertainties derived from a sensitivity analysis performed on three selected methods. There, variations in specific internal thresholds or parameters were deliberately applied. Specifically, the methods used in that work were: (i) the technique from Long and Ackerman (2000) and Long et al. (2006b), which uses broadband shortwave measurements, (ii) the techniques applied to measurements performed by MFRSR, which are described by Harrison et al. (1994) along with other references in Calbó et al. (2017a), and (iii) the analysis of images captured by RGB whole sky cameras, such as the Total Sky Imager (TSI, from Yankee Environmental Systems). Note that all of these methods are inherently limited to daytime periods.

The goal of the present research is to extend the work of Calbó et al. (2017a) to a method usable for both daytime and nighttime periods. A similar strategy to that of Calbó et al. (2017a) has been followed and applied here to a cloud detection method from surface measurements of downwelling longwave radiation (DLR), with the aim of estimating the frequency in the occurrence of conditions corresponding to the so-called transition zone between cloudy and cloud-free (though with some aerosol loading) skies.

Several atmospheric constituents affect the DLR reaching the surface such as water vapor, carbon dioxide, ozone, and other trace gases, as well as aerosol, which can emit and absorb in the longwave spectral range. Their vertical concentration profile, together with their spatial distribution over the surface, is very relevant. The temperature profile also determines the emission that occurs in different atmospheric layers and how DLR is distributed in the atmosphere. In general, for a cloudless atmosphere, water vapor content and temperature conditions at the lower layers of the atmosphere (i.e., close to the surface) are the main determinants of DLR reaching the ground (Viúdez-Mora et al., 2009).

On the other hand, clouds, through absorption and emission by their constituent water droplets or ice particles, have an observable impact on DLR reaching the surface (for a sensitivity analysis, see Viúdez-Mora et al., 2015). The main variation in DLR introduced by clouds is caused by the effects in the atmospheric window (the spectral band between 8 and 14 μm). Further, the high spatial and temporal variability of cloudiness, including both horizontal inhomogeneity (from scattered-to-broken clouds to overcast skies) and cloud vertical structure, has its corresponding effect on the variability of the DLR reaching the surface at any point. Consequently, DLR observed at surface can be used to detect clouds, and even to characterize cloud cover (Dürr and Philipona, 2004).

The DLR density flux (irradiance) incident onto a horizontal plane (hereafter denoted by $LW\downarrow$) can be routinely measured with pyrgeometers. Subsequently, the DLR effect due to cloudiness can be quantified by comparing actual (measured) $LW\downarrow$ with the corresponding estimation for an otherwise equivalent cloud-free atmosphere. This can be computed, to a certain degree of accuracy, by radiative modeling if the actual atmospheric temperature and water profiles are known or simulated (see, for example, Viúdez-Mora et al., 2009). Since these profiles are scarcely measured, several papers (see, for example, Brunt, 1932; Brutsaert, 1975; Ohmura, 1982; Andreas and Ackley, 1982; Guest, 1998) suggest that $LW\downarrow$ for cloud-free conditions can be estimated from air temperature and water content at screen level due to their close relationship with atmospheric conditions at lower layers, from which $LW\downarrow$ mainly originates. Information on cloudiness could thus be retrieved by comparison of measurements with parameterized clear sky $LW\downarrow$. However, here we have preferred to use a method specifically developed to characterize cloudiness; that of Dürr and Philipona (2004). This method includes estimating long-term (annual) and short-term (daily) clear sky $LW\downarrow$ evolutions, using a local empirical adjustment. This adjustment depends, at the end, on a single parameter, which is particularly convenient for the main objective of the present study: the assessment of the frequency in the occurrence of conditions associated to the transition zone.

2. Cloud detection

In this study, the method described by Dürr and Philipona (2004) to detect clouds from DLR has been applied to two years (2018 and 2019) of surface measurements of downwelling longwave irradiance, $LW\downarrow$, taken at the station located at the Polytechnic School of the University of Girona (41.962°N, 2.829°E, 115 m a.s.l.), in the northeast of the Iberian Peninsula. It should be stressed that the present work is not devoted to applying the whole APCADA (Automatic Partial Cloud Amount Detection Algorithm) method, which is dedicated to assessing cloud cover (Section 4.5 in Dürr and Philipona, 2004). Here, only the Cloud-Free Index as defined in Section 4.2 in Dürr and Philipona (2004) is used.

2.1. Data

At the Girona station, $LW\downarrow$ measurements are performed with a CGR4 pyrgeometer from Kipp&Zonen (Delft, The Netherlands), which is continuously shadowed by a device mounted on a solar tracker. Information on other variables measured at the station, along with routine maintenance tasks, can be found in Calbó et al. (2017b). Specifically, $LW\downarrow$ is measured at 1-s intervals, whereas 1-min averages are stored in the database. The pyrgeometer is recalibrated every two years at the manufacturer's facilities to obtain its sensitivity. For this study the relevant sensitivity values are 12.46, 12.64 and 12.62 W m^{-2} mV^{-1}, obtained from calibrations performed at the end of 2016, 2018 and 2020, respectively, thus within a range of <2% of the central value. Despite this low range of variation, daily sensitivity constants obtained by linear interpolation between calibrations were used to calculate $LW\downarrow$. In addition, the maintenance of the pyrgeometer follows the main recommendations: periodic calibration traceable to the World Infrared Standard Group (WISG) of pyrgeometers at PMOD/WRC (Davos, Switzerland), ventilation and continuous shadowing, daily cleaning, and supervision of retrieved data. Therefore, we are confident that the measurements are sufficiently accurate for the purpose of this work, with uncertainties in the order of a few W m^{-2}.

The method for cloud detection also requires air temperature and relative humidity (T_a and RH) at the location of $LW\downarrow$ measurements. These variables are measured with a Vaisala HM35AC probe (using a Pt-100 resistor for temperature and a HUMICAP sensor for relative humidity). Measurements are performed at 1-s intervals and stored in 5-min averages.

The stored values of $LW\downarrow$, air temperature and humidity were averaged in 10-min intervals (as prescribed in Dürr and Philipona, 2004) to build the dataset for this study. For the two years considered, >95,000 cases were used (corresponding to >90% of the 105,120 possible cases over a two-year period). Data gaps, around 9% of the possible cases, correspond mainly to the calibration period at the end of 2018.

Other measurements and observations were helpful to check the sky conditions for this study. At the station, solar direct normal and diffuse horizontal irradiances (DNI and DHI), respectively, are measured with a pyrheliometer (CH1, from Kipp&Zonen) and a pyranometer (CM11, also from Kipp&Zonen) mounted on a solar tracker with a shadowing device. A digital camera (SONA, from Sieltec Canarias) takes hemispherical images of the sky. Programmed exposure allows image acquisition during both daylight and nighttime periods. Both irradiance measurements and camera observations are stored in 1-min periods. Besides this, a ceilometer (CL31, from Vaisala) allows for the backscatter profile to be obtained, from which the cloud base is derived with a built-in algorithm. A summary of all the observations and instruments involved is displayed in Table 1.

2.2. Method

The Dürr and Philipona (2004) method (hereinafter referred to as DP2004) is intended to detect clouds based on $LW\downarrow$, air temperature and water vapor pressure right at the Earth's surface (screen level). First, the Cloud-Free Index (CFI) is defined as:

$$CFI = \frac{\epsilon_A}{\epsilon_{AC}} \tag{1}$$

with ϵ_A being the apparent emissivity of the sky, and ϵ_{AC} the corresponding emissivity for an equivalent cloud-free atmosphere, which is considered a grey body. The apparent emissivity of the sky is defined as:

$$\epsilon_A = \frac{LW\downarrow}{\sigma T_a^4} \tag{2}$$

where σT_a^4 is the blackbody thermal emittance, σ is the Stefan-Boltzmann constant, and T_a is the absolute air temperature. Thus, CFI can be expressed as:

$$CFI = \frac{LW\downarrow}{\epsilon_{AC}\sigma T_a^4} \tag{3}$$

Sufficiently thick clouds exhibit an emissivity approaching that of the blackbody, i.e., unity. Consequently, cloudy conditions lead to a higher $LW\downarrow$ than clear sky conditions do, so the CFI becomes >1. This value can therefore be used as a threshold for cloudiness detection: CFI $\leq$ 1 represents cloud-free conditions, and CFI > 1 cloudy conditions.

In DP2004, ϵ_{AC} is calculated as:

$$\epsilon_{AC} = \epsilon_{AD} + [k(t) + \Delta k(t)]\left(\frac{e}{T_a}\right)^{1/7} \tag{4}$$

where ϵ_{AD} is an altitude-dependent emissivity of a completely dry atmosphere. Its value for the Girona station (115 m above sea level) has been estimated by linearly extrapolating the results obtained (using radiative modeling) by Marty and Philipona (2000), for stations at different altitudes. Fig. 1 shows those ϵ_{AD} values plotted against altitude, together with the estimate of 0.233 for Girona.

In the second term of Eq. 4, e is the water vapor pressure (in Pa), which can be calculated from air temperature and relative humidity RH. The time-dependent site-specific functions $k(t)$ and $\Delta k(t)$ approximate the effects of both diurnal and annual cycles of clear-sky emissivity that are connected to the temperature vertical profile near the surface during nighttime and daytime and aim to describe the effects of variations with respect to the standard lapse rate (Marty and Philipona, 2000). To the base evolution function $k(t)$, a time-dependent shift function $\Delta k(t)$ is

Table 1
Measurements used and details of the instruments deployed at the Girona station.

Measurement	Abbreviation	Instrument	Acquisition rate	Aggregation for this study
Surface downwelling longwave irradiance	$LW\downarrow$	Kipp-Zonen CGR4	1 s	10 min
Air temperature	T_a	Vaisala HM35AC probe	1 s	10 min
Air relative humidity	RH	Vaisala HM35AC probe	1 s	10 min
Solar (shortwave) direct normal irradiance	DNI	Kipp&Zonen CH1 pyrheliometer	1 s	1 min
Solar (shortwave) diffuse horizontal irradiance	DHI	Shadowed Kipp&Zonen CM11 pyranometer	1 s	1 min
Cloud detection		Vaisala CL31 ceilometer	16 s	10 min
Sky images		SONA Sieltec Canarias hemispherical camera	1 min	

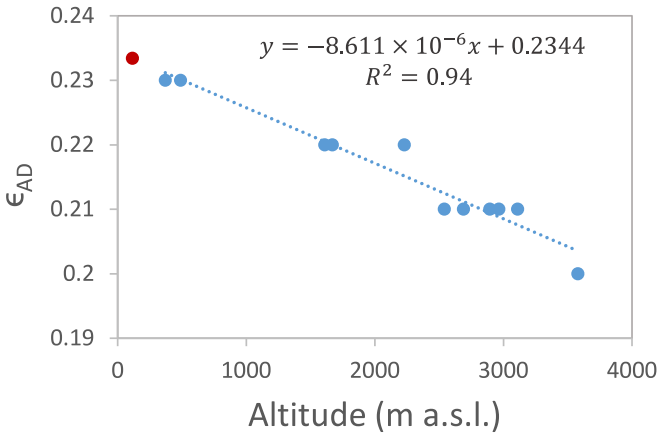

Fig. 1. Dependence of the calculated emissivity for a completely dry atmosphere on altitude (blue dots), according to the results shown in Table 2 of Marty and Philipona (2000), together with the corresponding linear fit. The red dot represents the extrapolation to the altitude of the Girona station (115 m a.s.l.) from which measurements for the present study have been taken. (For interpretation of the references to colour in this figure legend, the reader is referred to the web version of this article.)

added to constrict the cloudiness detection to a selected confidence level (CL; see below). In the original method, $k(t)$ takes the form:

$$k(t) = \bar{k}_i + k_{i,amp} cos\left(\frac{2\pi}{24}t - \frac{\pi}{4}\right) \quad (5)$$

to describe the diurnal cycle, with t in hours. The $-\pi/4$ term applies a 3-h phase shift to the diurnal evolution due to the expected time lag between maximum irradiance and lapse rate. However, the time shift used in the present work was modified to zero to better adjust to the local diurnal cycle based on the climatology of the Girona station. A full description of the estimation of the phase shift can be found in the Appendix. The term $\bar{k}_i$ and the factor $k_{i,amp}$ evolve, in turn, on an annual cycle according to the day of the year i. They are defined as:

$$\bar{k}_i = \frac{k_{i,night} + k_{i,day}}{2} \quad (6)$$

$$k_{i,amp} = \frac{k_{i,night} - k_{i,day}}{2} \quad (7)$$

with

$$k_{i,night} = \frac{1}{2}\left(k_{night,winter} + k_{night,summer}\right) + \frac{1}{2}\left(k_{night,winter} - k_{night,summer}\right) cos\left(\frac{2\pi}{365}i - \frac{\pi}{4}\right) \quad (8)$$

$$k_{i,day} = \frac{1}{2}\left(k_{day,winter} + k_{day,summer}\right) + \frac{1}{2}\left(k_{day,winter} - k_{day,summer}\right) cos\left(\frac{2\pi}{365}i - \frac{\pi}{4}\right) \quad (9)$$

For leap years, the period would be 366 days. In Eqs. 8 and 9 the term $-\pi/4$ applies a phase shift of 1.5 months in the annual evolution of $k(t)$, which was also used for the Girona station in accordance with its climatology. Thus, four parameters ($k_{night,summer}$, $k_{night,winter}$, $k_{day,summer}$ and $k_{day,winter}$) determine the time evolution of $k(t)$. A formulation like that in Eqs. 5–9 is used to calculate $\Delta k(t)$ from four other parameters: $\Delta k_{night,summer}$, $\Delta k_{night,winter}$, $\Delta k_{day,summer}$ and $\Delta k_{day,winter}$. It is sufficient to change any k by Δk in Eqs. 5–9 to obtain the analogous formulation for $\Delta k(t)$. It should be noted that some details of the notation have been slightly adapted here from that in DP2004.

Determining the eight parameters needed to calculate the site-specific functions $k(t)$ and $\Delta k(t)$ is based on fitting over four selected datasets corresponding to *night-winter*, *day-winter*, *night-summer*, and *day-summer*, all under cloud-free conditions. Specific values of k and Δk are found from the fitting at the diurnal and annual minima and maxima of the lapse rate, taken during the afternoon (day) and early morning (night) for the diurnal extrema, and in June–September (summer), and December–March (winter) for the annual extrema.

The Appendix provides some more details on how the cloud-free cases were filtered to build the four datasets, how the fit was performed and how the parameters describing $k(t)$ and $\Delta k(t)$ were retrieved. In particular, the Appendix includes the different values taken by the parameters that describe the function $\Delta k(t)$, depending on several confidence levels (CL) applied to the cloudiness detection: 80%, 90% (the original value in DP2004), 95% and 99%. Specifically, the effect of the confidence level is a change in the values of Δk. The latter value acts upon the value of k obtained from fitting a function to the cloud-free cases previously selected. When $k + \Delta k$ is used in the function, the result is that the fitted function is displaced toward higher values of apparent emittance. Finally, this displaced curve defines which samples are left in or out (that is, which samples will be considered cloud-free or cloudy when we later apply the CFI <> 1 threshold).

A flow chart summarizing the method is presented in Fig. 2. To sum up, we are applying a cloudiness detection based on a threshold for *CFI* (Eq. 3), i.e., CFI > 1, which depends on the apparent cloud-free emissivity ϵ_{AC} and, therefore, on the time-dependent parameters included in Eq. 4. Ultimately, this function depends on the confidence level selected for cloudiness detection (90% in DP2004) through the values of Δk. In other words, the selected confidence level, which is somewhat arbitrary, introduces an inherent uncertainty in the method, which mainly affects cloudiness detection in boundary (between cloudy and cloud-free) situations.

Of course, apart from the uncertainty introduced by the confidence level selected in the cloudiness detection, several causes of uncertainty

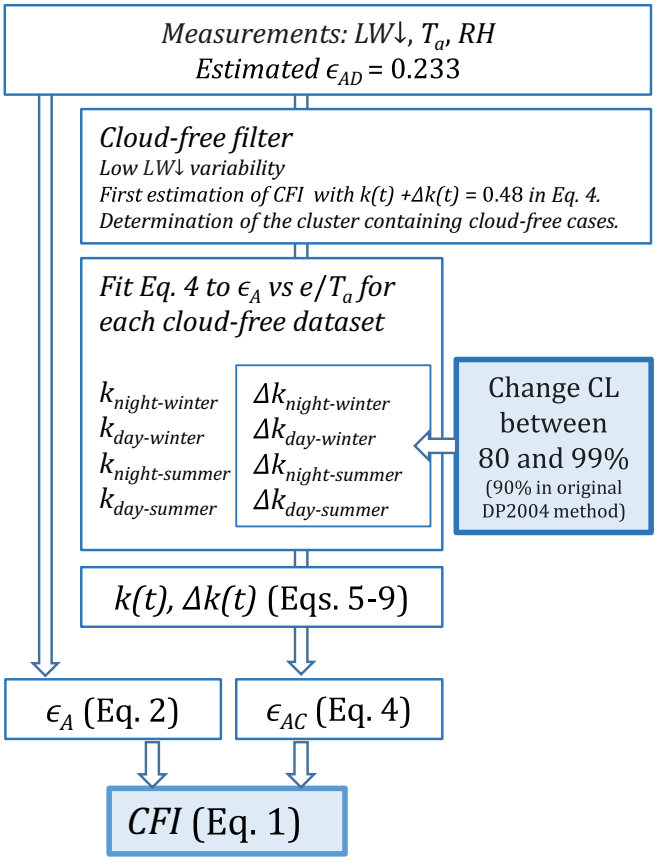

Fig. 2. Flow chart summarizing the DP2004 method and how the change in confidence level of cloudiness detection affects the *CFI* calculation.

remain: those corresponding to the measurements ($LW\downarrow$, T_a and RH), to the determination of ϵ_{AD}, to the form of Eqs. 4–9, and to the procedure used for the initial selection of clear-sky cases for the function fits (indeed other methods could be used for this selection, the most obvious being the direct visual inspection of the sky if possible).

3. Results and discussion

3.1. Method performance

After applying the Dürr and Philipona (2004) method (briefly described in Section 2, and in the Appendix), the evolution of *CFI* over the course of the two years of data was obtained. First, however, in Fig. 3a we show the evolution of $LW\downarrow$, together with the corresponding evolution of the estimated cloud-free value, $\epsilon_{AC}\sigma T_a^4$ (for 90% CL), obtained using Eqs. 4—9, over the years 2018 and 2019. Meanwhile, Fig. 3b shows the difference between the two quantities. The evolution of $\epsilon_{AC}\sigma T_a^4$ follows the annual cycle of the measurements reasonably well in the low range of $LW\downarrow$ values, as is expected for cloud-free cases. Thus, many differences are slightly negative (corresponding to clear skies), whereas the largest positive differences indicate the presence of clouds that enhance the emission of LW radiation.

Next, some examples of the DP2004 method's short-term performance are presented. Fig. 4 shows a set of periods selected to illustrate the method's capability in detecting cloudiness. To this aim, the evolution of several variables is shown (at the 10-min time resolution): $LW\downarrow$, *CFI* for 90% CL in cloudiness detection, direct normal and diffuse horizontal shortwave irradiances (*DNI* and *DHI*), and the occurrence of detection of clouds by the ceilometer within each 10-min interval. It should be noted, firstly, that the ceilometer can only detect clouds in the pointing (vertical) direction and is limited up to a nominal maximum distance (height) of about 7 km. Secondly, that the use of shortwave irradiances is, of course, limited to diurnal periods, when the Sun is above the horizon. Despite their limitations, these variables can be helpful in identifying cloudiness and characterizing sky conditions. Inspection of the images taken by the hemispherical camera can further confirm the presence of clouds.

The first period selected (see Fig. 4a) lasts 48 h: starting at 0000 UTC on 2018/05/01. An initial cloudy period extends throughout the first day shown, with cloudiness disappearing at about 1700 UTC. A long cloudless period then follows, lengthening from the evening of 2018/05/01 until the afternoon of 2018/05/02, except for a short interruption around 0400 UTC on 2018/05/02 (as detected by the DP2004 method). Clouds reappear around 1700 UTC on 2018/05/02. During daylight cloudy periods, the low values of *DNI* (often down to near zero values) reveal sun occultation by clouds. High *DHI* (caused by radiative scattering) also reveals the presence of clouds over the same periods. Contrary to this, cloudless conditions throughout the morning of 2018/05/02 lead to high *DNI* and very low *DHI*. The evolution of the sky conditions over the entire period selected derived from measurements of irradiances, is confirmed by inspecting the images taken by the hemispherical camera (see some examples in Fig. 4c). In addition, the ceilometer corroborates the presence of clouds at least in the vertical direction for the two long cloudy periods described.

The detection of cloudy periods by means of *CFI* computed in accordance with DP2004 (with 90% CL) is quite correct for this selected two-day period: *CFI* takes values >1 throughout the two long cloudy periods described. Even other short periods showing cloud presence can be detected. For instance, the brief drop in the *DNI* (combined with the increase in the *DHI*) around 1530 UTC on 2018/05/02 (see the corresponding sky image in Fig. 4c). Before that (i.e., throughout the morning and early afternoon), *CFI* was steadily increasing, until clouds appeared, even over the vertical of the site, as revealed by ceilometer observations.

As expected, the agreement between methods for detecting cloud occurrence is not perfect. This can been see in both Fig. 4a and b. Sometimes, the DP2004 method detects clouds, and the ceilometer does not, as in the case of the *CFI* peak at 0220 UTC on 2018/06/18. Other times, the DP2004 method fails to detect cloudiness. For example, shortwave irradiances show evolutions and temporal variability indicating the presence of clouds for several hours around noon on 2018/06/18 (decreased *DNI* and relatively high *DHI*, and the presence of high thin clouds confirmed by the camera imagery) but the DP2004 method only detects cloudiness for a relatively short interval. On the other hand, cloud detection from the DP2004 method (for 90% CL) and ceilometer

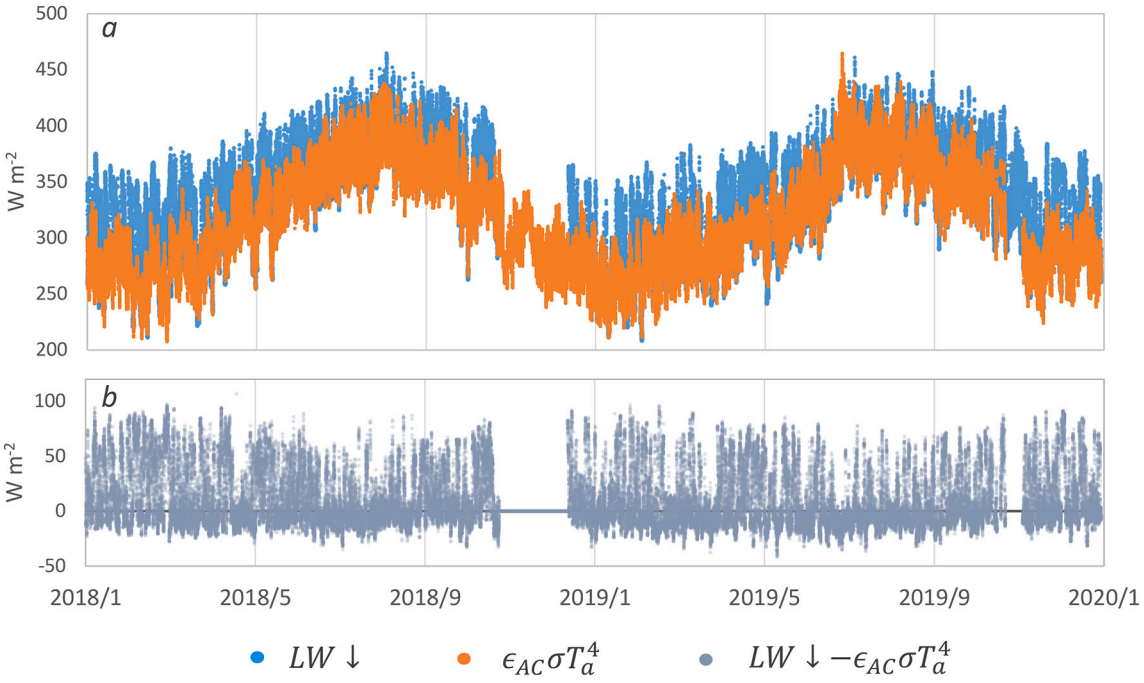

Fig. 3. (a) Evolution over the 2018–2019 period of $LW\downarrow$ measurements (blue; 10-min averages) and the estimated cloud-free value $\epsilon_{AC}\sigma T_a^4$ (orange; 90% CL). Note the gap in the measurements of $LW\downarrow$ in fall 2018, due to a pyrgeometer calibration period. (b) Evolution of the difference between $LW\downarrow$ and $\epsilon_{AC}\sigma T_a^4$ (grey). (For interpretation of the references to colour in this figure legend, the reader is referred to the web version of this article.)

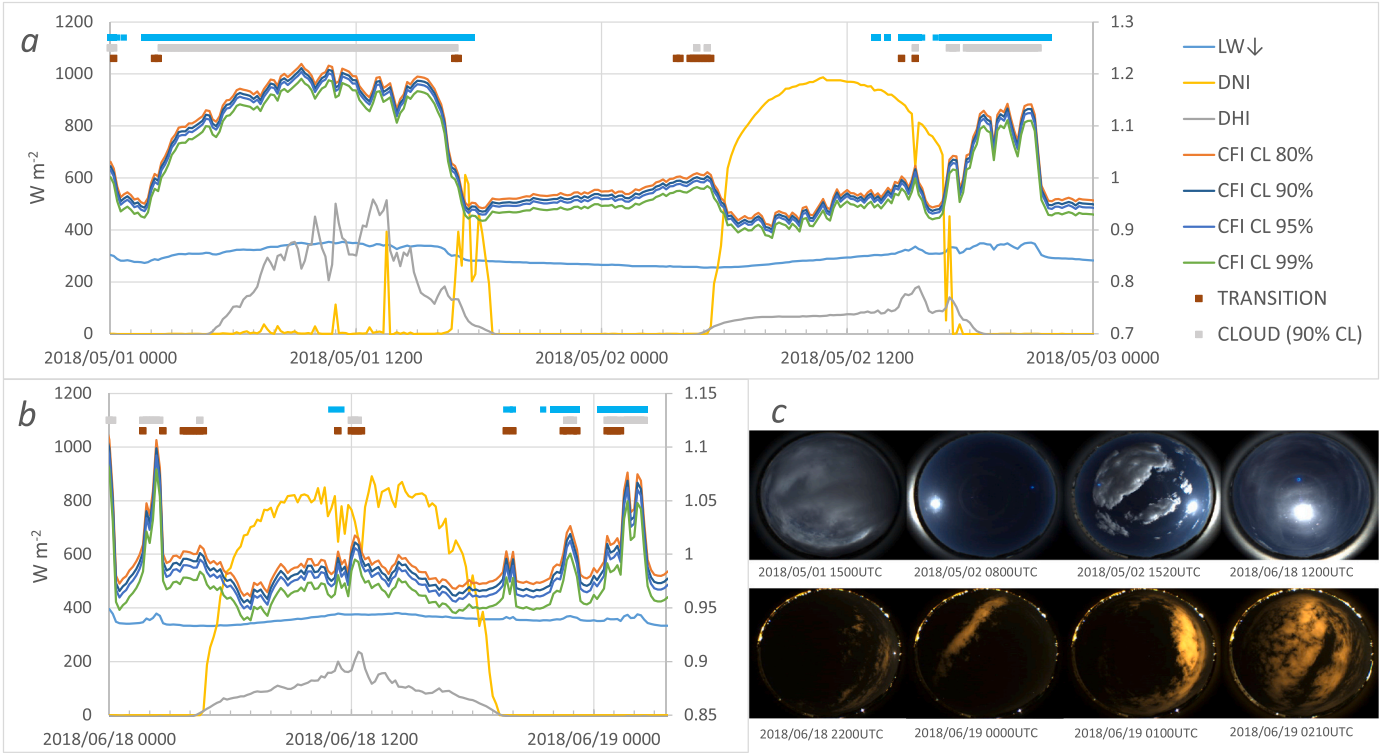

Fig. 4. (a) Evolution over a two-day period (2018/05/01 and 2018/05/02) of several magnitudes, either measured or computed: downwelling longwave irradiance *LW*↓, shortwave direct normal irradiance *DNI*, shortwave horizontal diffuse irradiance *DHI*, *CFI* calculated for several confidence levels in cloudiness detection (80%, 90%, 95% and 99%). Irradiances are referenced to the left axis scale, whereas computed *CFI* are referenced to the right axis scale. Ceilometer cloud detection over 10-min periods is indicated by thick blue blocks at the top of the plot. Similarly, cloud detection by DP2004 method (90% CL) is indicated by thick grey blocks. Transition-zone conditions periods, as defined in Section 3.2, are indicated by thick purple blocks. (b) The same as in (a) but for a selected period within days 2018/06/18 and 2018/06/19. Note the different scales (right axes) to represent *CFI* in (a) and (b). (c) Some sky images taken by the hemispherical camera corresponding to these two periods. All time specifications correspond to Coordinated Universal Time (UTC). (For interpretation of the references to colour in this figure legend, the reader is referred to the web version of this article.)

are quite consistent for two short intervals of cloudiness during the same nighttime period (18/06/2018 at 2230 UTC and 2018/06/19 at 0210 UTC).

Of course, to explain some of the discrepancies between methods one must first consider the different field of view each instrument has: whole sky for the pyrgeometer (measuring downward longwave irradiance *LW*↓) and shadowed pyranometer (measuring shortwave *DHI*), and camera imagery; a narrow field of view in the vertical direction for the ceilometer, and in the Sun direction for the pyrheliometer (measuring *DNI*). In addition, some sensors suffer from distance limitations: the detection range of the ceilometer depends on the emitting power of the laser, whereas cloud observations with the camera (which is sensitive to the visible spectral range) at night needs some light source, either natural (from the Moon when it is above the horizon) or artificial (city lights). Even the illumination by artificial light has a distance limitation: high clouds are barely visible in the camera's nighttime images.

3.2. Transition conditions

Although the selection of a 90% CL (the original value in the DP2004 method) is generally used in case filtering, it introduces an inherent arbitrariness in the detection of cloudiness, as occurs in other techniques like those used by Calbó et al. (2017a). In the latter paper, for each technique, a set of threshold parameters was used to assess the uncertainty in cloud detection/evaluation associated with the transition zone between a cloudy and cloud-free sky. A similar procedure is used here to estimate the frequency in the occurrence of these transition conditions. Based on the selected detection method, we qualify some conditions as belonging to the transition zone between cloud and cloud-free sky when it meets or not the requirement ($CFI > 1$) depending on the value of the threshold (the confidence-level). Specifically, we consider that conditions for which

$$CFI \text{ at } 99\%CL < 1 < CFI \text{ at } 80\%CL \tag{10}$$

cannot be clearly qualified as either cloud-free or cloudy, and we assume that they could correspond to the transition zone between those pure cases. In other words, situations with $CFI < 1$, even at 80% CL, are definitely cloud-free cases, whereas situations with $CFI > 1$, even at 99% CL, must be necessarily cloudy. In this sense, it is worth noting that the aim of this work is not to analyze in detail what kind of conditions lead to the DP2004 method detecting transition periods, but it is interesting to see some examples showing how the method classifies some situations as belonging to transition periods, and how these situations are extended in time.

Following the previous definition of transition conditions, the evolutions shown as examples in Fig. 4a and b can be revisited. Thus, we have also indicated the transition periods (purple blocks at the top of each panel) according to the criterion stated in Eq. 10, and several different situations are observed. First, some transition periods clearly correspond to the beginning and end of cloudy periods, such as that of 2018/05/01 in which both transitions were relatively fast. Second, other very short transition periods (with the limitation of the 10-min resolution) can be observed at other times (around 1500 UTC on 2018/05/02 and 0200 UTC on 2018/06/18). Third, several longer transition periods, lasting up to one hour, are also observed, even in cases for which the ceilometer did not report cloud detection (e.g., the early morning of day 2018/05/02 or at 0400 UTC on 2018/06/18). Some conditions during the night between 2018/06/18 and 2018/06/19 are likewise labeled as

transition periods.

For the entire database, a total of 4126 transition periods have been found, ranging in duration from the 10-min resolution of the method up to several hours. Fig. 5 shows the distribution of the duration of the transition periods. Short periods (10-min) are the most frequent (1686 cases), constituting almost 41% of the total transition periods. These short periods, however, totalize <12% of the total transition time. The median of the transition duration is 20 min. Longer periods, lasting an hour or more, constitute about 17% of the transition periods. Overall, 15% of the time is spent in transition conditions. This is computed as the total time duration of the 4126 transition periods divided by the total length of the period analyzed (two years minus the missing data due to calibration).

3.3. Distribution of the Cloud-Free Index

The values of the *CFI* show a bimodal distribution for any selected confidence level in cloudiness detection, as can be seen in Fig. 6. A Gaussian peak-fitting analysis performed on the distribution for 90% CL gives a first peak centered at the value 0.985, with width 0.048, and a second peak centered at 1.088 with width 0.192. The two-peak fitting is very good, with a determination coefficient of 0.995. Moreover, Fig. 6 highlights the strong overlying between the two modes of the distribution. Changing the confidence level in the cloudiness detection method mainly affects the center of the distribution, but not its width. A straightforward interpretation of the bimodal behavior as corresponding to cloud-free and cloudy situations (first and second peaks, respectively) would lead to interpreting the overlying region as that connected to transition cases.

An estimate of the frequency in the occurrence of transition conditions can be derived from the distributions shown in Fig. 6. For the analyzed database, and for a 90% CL in cloudiness detection, 47% of the 10-min registers have a *CFI* lower than 1 and, therefore, are qualified as corresponding to cloud-free conditions. From this value we can derive that 53% of the cases have cloudiness. This value is consistent with the cloudiness (mean cloud cover) obtained at the same measurement station in other studies (Calbó and Sanchez-Lorenzo, 2009).

As stated above, changing the confidence level in cloudiness detection modifies the distribution of *CFI*: 80% CL, 95% CL and 99% CL lead to 42%, 51% and 57%, respectively, of cloud-free cases. The difference between the cloud-free cases for the extreme values of confidence level, i.e., 80% and 99%, is 15%, obviously the same occurrence as obtained above after the analysis of the duration of transition zone situations (at the end of Section 3.2). This value would constitute the fraction of cases that cannot be clearly classified as either cloudy or cloud-free as *CFI* values depend on the confidence level assumed in the DP2004 method within the range 80–99%. Of course, a stricter CL range would reduce

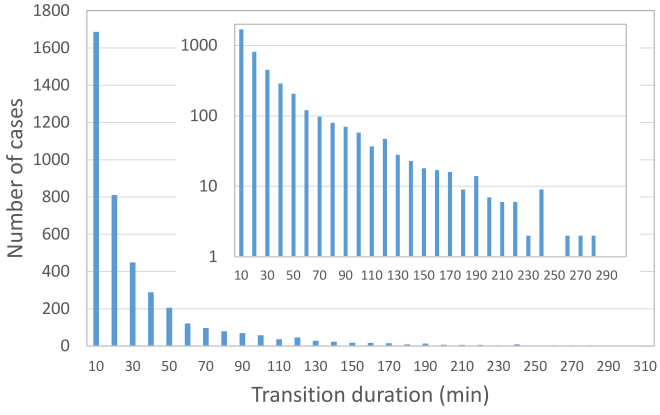

Fig. 5. Distribution of the duration of the transition periods, for the whole database. Inset: the same but in logarithmic scale.

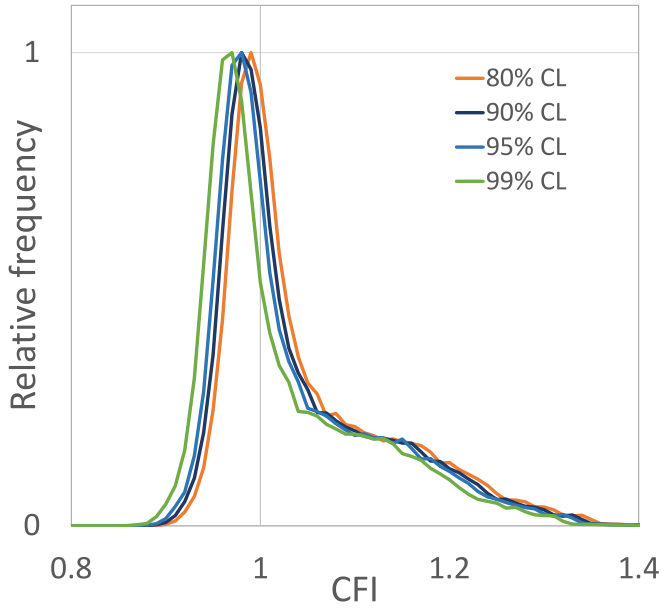

Fig. 6. Distribution of the *CFI* depending on the confidence level (CL) selected for cloudiness detection. Curves are normalized to their corresponding maximum.

the estimation of the occurrence of transition conditions. For example, the 90–99% range would give a 10% occurrence of transition conditions. As a conclusion, based on the DP2004 method applied, we consider 10–15% to be a reasonable range for the occurrence of cloud-free to cloudy transition conditions in the analyzed data.

4. Concluding remarks

The methodology from Dürr and Philipona (2004) was applied to two years (2018 and 2019) of downwelling longwave irradiance measured with a pyrgeometer at Girona (northeast of the Iberian Peninsula). The method defines the Cloud-Free Index (*CFI*) as the ratio between the irradiance measured for any sky condition (ranging from cloud-free to cloudy) and that corresponding to the otherwise cloudless atmosphere. The emissivity of the cloudless atmosphere is estimated through an empirical method that implies a fitting to four sets of selected cloudless cases for combined winter/summer and day/night periods. The possibility of varying the confidence level in the tuning for cloudiness detection in those four datasets implies changes in the conditions labeled as cloud-free or cloudy, therefore allowing for the frequency in the occurrence of the transition zone (i.e., conditions between cloud-free and cloudy) to be estimated. For this work, the phase in the sinusoidal function that describes the diurnal period of cloud-free emissivity was changed with respect to that proposed in Dürr and Philipona (2004), to obtain a better fit to the measurements taken at Girona.

A median duration of 20-min is obtained for the transition periods found in this study (which is performed on a 10-min time resolution dataset). Shorter transitions (occurring in only 10-min) are the most frequent, but transitions lasting several hours are also detected.

The Cloud-Free Index shows a bimodal distribution with a strong overlap between modes. This overlap could be revealing the contribution of transition conditions to the *CFI* distribution. The analysis of the *CFI* for the two years of data treated indicates that about 10–15% of the time the sky conditions could be associated with the transition between cloud-free and cloudy sky. This result is found by analyzing the changes in the distribution of the *CFI* when the confidence level in cloudiness detection (a single parameter) is modified. The 10–15% range is close to results derived in previous works using methods focused on the shortwave band (Calbó et al., 2017a), and satellite observations in the

longwave band (Schwarz et al., 2017). Even higher estimates of the occurrence of the transition zone are given in Koren et al. (2007).

As stated in the Introduction, any cloud detection method is potentially suitable for estimating the frequency in the occurrence of transition conditions between clouds and cloud-free air with the methodology applied here. For this, some reasonable change in the tuning parameters for cloudiness detection must be possible. The extension of methods for estimating the occurrence of transition conditions (or the spatial extent of the transition region) is largely significant, given the importance of clouds' effects on the climate balance.

The extent to what transition conditions could be present in the atmosphere points to a non-negligible effect in the global climate balance, which should be taken into account when assessing the already high uncertainties in the effects of cloudiness. Further efforts should be devoted to evaluating the extent to what different methodologies coincide when qualifying atmospheric conditions as belonging to the transition zone, and to establish a range of optical depths corresponding to these conditions.

CRediT authorship contribution statement

Josep-Abel González: Conceptualization, Methodology, Data curation, Formal analysis, Writing – review & editing, Visualization, Project administration, Funding acquisition. **Josep Calbó:** Conceptualization, Methodology, Writing – review & editing, Project administration, Funding acquisition. **Yolanda Sola:** Conceptualization, Methodology, Writing – review & editing, Visualization.

Declaration of Competing Interest

The authors declare that there is no competing interest.

Data availability

The datasets generated and/or analyzed during the study are available from the corresponding author on reasonable request.

Acknowledgements

The authors appreciate the assistance of Jaume Ruiz de Morales who treated the ceilometer data. The study has been funded through project NUBESOL-2 (PID2019-105901RB-I00) of the Spanish Ministry of Science and Innovation (MICINN). The authors also appreciate the valuable comments of the reviewers which have helped to improve the manuscript.

Appendix

Section 4.4 in Dürr and Philipona (2004) shows an example of how the adjustment of the $k(t)$ and $\Delta k(t)$ functions is performed for *day-winter* cases. The selection of cloud-free cases for the adjustment starts with the use of the standard deviation (*Stdev*) of $LW\downarrow$ calculated over 2 h around 1530 UTC, hence 3 h ($\pi/4$) after the average noontime in Switzerland. Only cases with $Stdev \leq 1$ W m^{-2} are considered. These cases of low variability in $LW\downarrow$ (note that there is one datum every 10 min) might correspond to both overcast and cloud-free cases, but plotting a first estimation of the *CFI* based on Eq. 4 with a guess value of 0.480 for $[k(t) + \Delta k(t)]$ results in two clusters of samples which are obviously separated; therefore, an upper limit of the *CFI* can be obtained to separate cloud-free from cloudy cases.

For the present work, we modified the phase shift in Eq. (5) to better describe the local diurnal cycle of the derived sky apparent emissivity for the database used, since it is expected that the climatology in Girona differs from the stations used in the work of Dürr and Philipona (2004). To select a suitable phase, we plotted the value of the factor $k(t) + \Delta k(t)$ of Eq. (5) versus time for all data (Fig. A1a). The factor was computed from the ratio $(\epsilon_A - \epsilon_{AD})/(e/T_a)^{1/7}$, where we used ϵ_A instead of ϵ_{AC} since not only cloud-free situations were considered. From this plot, a phase of 0 (corresponding to 0000 UTC for nighttime cases and 1200 UTC for diurnal cases) was selected to perform the diurnal cycle fit of k(t) + Δk(t). In fact, values within the intervals 2340—0020 UTC (centered at 0000 UTC) and 1140—1220 UTC (centered at 1200 UTC) were used in the fitting for the nighttime and daytime periods, respectively (Fig. A1b).

The *CFI* upper limits obtained after the previously explained treatments were 1.03, 0.92, 1.01 and 0.93, respectively, for the four datasets corresponding to *night-winter*, *day-winter*, *night-summer*, and *day-summer* cloud-free conditions.

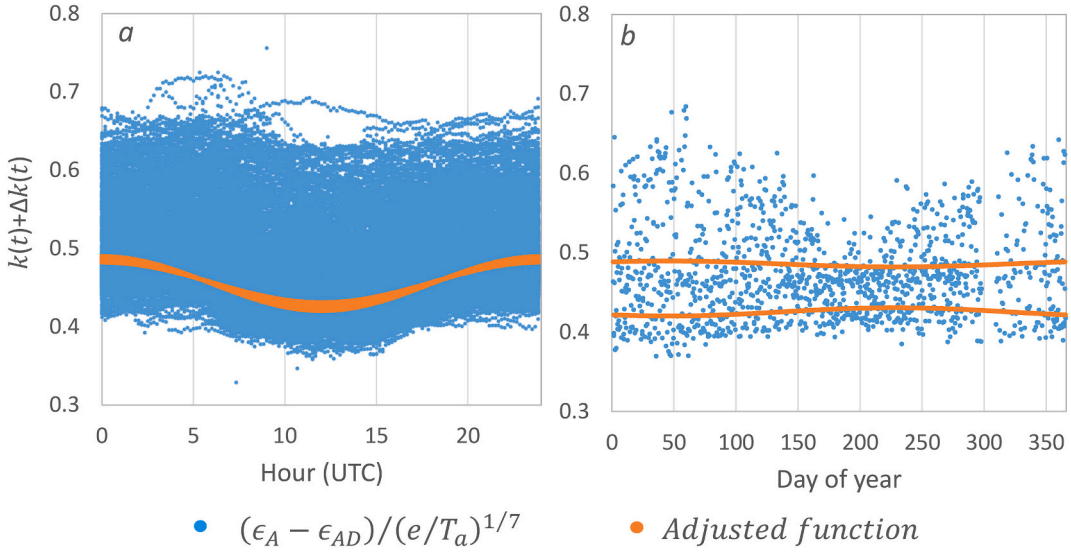

Fig. A1. (a) Diurnal evolution of the factor $k(t) + \Delta k(t)$ estimated from the ratio $(\epsilon_A - \epsilon_{AD})/(e/T_a)^{1/7}$ for all data (blue dots) and the adjusted $k(t) + \Delta k(t)$ function (orange dots) for 90% CL in cloudiness detection. (b) Yearly evolution of the same quantities, but only for 0000 UTC and 1200 UTC. (For interpretation of the references to colour in this figure legend, the reader is referred to the web version of this article.)

For each of the four datasets, the apparent emissivity ϵ_A ($LW\downarrow/\sigma T_a^4$) is plotted against the ratio e/T_a (i.e., the basis of the last term in Eq. 4). The function in Eq. 4 is then fitted to the data, assuming $\Delta k(t) = 0$, to obtain $k_{day,winter}$ (in the example in Dürr and Philipona, 2004). On the other hand, the value of $\Delta k_{day,winter}$ is obtained as the difference between the function and the upper 90% confidence level (CL) of the fit, evaluated for the average value of e/T_a. The same procedure is applied to the *night-winter*, *night-summer*, and *day-summer* datasets. In Table A1, the second and fourth columns show, respectively, the values of k and Δk, the latter for the 90% CL (the default confidence level for cloud detection in DP2004 method) of the fit for each of the four clear-sky datasets from the Girona station. The other columns show the values of Δk obtained when the CL for cloudiness detection is adjusted to 80%, 95% and 99%. Values of Δk increase monotonically with CL, so in this way ϵ_{AC} is also increased (and the calculated CFI, decreased), finally inducing a lower detection of cloudy cases, which will result in greater likeliness of these cases actually being cloudy.

Table A1
Values of k and Δk obtained for Girona, for the different confidence levels for the detection of cloudiness situations in the four reference datasets. The values retrieved with the original 90% CL in DP2004 are in boldface.

Cloud-free dataset	k	Δk / 80% CL	Δk / 90% CL	Δk / 95% CL	Δk / 99% CL
Night-winter	0.4609	0.0224	0.0288	0.0344	0.0453
Day-winter	0.4016	0.0147	0.0189	0.0225	0.0297
Night-summer	0.4632	0.0149	0.0191	0.0228	0.0301
Day-summer	0.4146	0.0127	0.0163	0.0195	0.0258

References

Andreas, E.L., Ackley, S.F., 1982. On the differences in ablation seasons of Arctic and Antarctic Sea ice. J. Atmos. Sci. 39 (2), 440–447. https://doi.org/10.1175/1520-0469(1982)039<0440:OTDIAS>2.0.CO;2.

Brunt, D., 1932. Notes on radiation in the atmosphere. I. Q. J. Roy. Meteor. Soc. 58 (247), 389–420. https://doi.org/10.1002/qj.49705824704.

Brutsaert, W., 1975. On a derivable formula for long-wave radiation from clear skies. Water Resour. Res. 11 (5), 742–744. https://doi.org/10.1029/WR011i005p00742.

Calbó, J., Sanchez-Lorenzo, A., 2009. Cloudiness climatology in the Iberian Peninsula from three global gridded datasets (ISCCP, CRU TS 2.1, ERA-40). Theor. Appl. Climatol. 96, 105–115. https://doi.org/10.1007/s00704-008-0039-z.

Calbó, J., Long, C.N., González, J.A., Augustine, J., McComiskey, A., 2017a. The thin border between cloud and aerosol: Sensitivity of several ground based observation techniques. Atmos. Res. 196, 248–260. https://doi.org/10.1016/j.atmosres.2017.06.010.

Calbó, J., González, J.A., Sanchez-Lorenzo, A., 2017b. Building global and diffuse solar radiation series and assessing decadal trends in Girona (NE Iberian Peninsula). Theor. Appl. Climatol. 129 (3), 1003–1015. https://doi.org/10.1007/s00704-016-1829-3.

Charlson, R.J., Ackerman, A.S., Bender, F.A.M., Anderson, T.L., Liu, Z., 2007. On the climate forcing consequences of the albedo continuum between cloudy and clear air. Tellus 59B, 715–727. https://doi.org/10.1111/j.1600-0889.2007.00297.x.

Chiu, J.C., Marshak, A., Knyazikhin, Y., Pilewski, P., Wiscombe, W.J., 2009. Physical interpretation of the spectral radiative signature in the transition zone between cloud-free and cloudy regions. Atmos. Chem. Phys. 9 (4), 1419–1430. https://doi.org/10.5194/acp-9-1419-2009.

Clothiaux, E.E., Miller, M.A., Perez, R.C., Turner, D.D., Moran, K.P., Martner, B.E., Ackerman, T.P., Mace, G.G., Marchand, R.T., Widener, K.B., Rodriguez, D.J., Uttal, T., Mather, J.H., Flynn, C.J., Gaustad, K.L., Ermold, B., 2001. The ARM Millimeter Wave Cloud Radars (MMCRs) and the Active Remote Sensing of Clouds (ARSCL) value added product (VAP). DOE Office of Science Atmospheric Radiation Measurement (ARM) user facility, United States. https://doi.org/10.2172/1808567.

Costa-Surós, M., Calbó, J., González, J.A., Long, C.N., 2014. Comparing the cloud vertical structure derived from several methods based on radiosonde profiles and ground-based remote sensing measurements. Atmos. Meas. Tech. 7 (8), 2757–2773. https://doi.org/10.5194/amt-7-2757-2014.

Di Girolamo, L., Davies, R., 1997. Cloud fraction errors caused by finite resolution measurements. J. Geophys. Res. Atmos. 102 (D2), 1739–1756. https://doi.org/10.1029/96JD02663.

Dubovik, O., King, M.D., 2000. A flexible inversion algorithm for retrieval of aerosol optical properties from Sun and sky radiance measurements. J. Geophys. Res. Atmos. 105 (D16), 20673–20696. https://doi.org/10.1029/2000JD900282.

Dürr, B., Philipona, R., 2004. Automatic cloud amount detection by surface longwave downward radiation measurements. J. Geophys. Res. Atmos. 109 (D5), D05201. https://doi.org/10.1029/2003JD004182.

Eytan, E., Koren, I., Altaratz, O., Kostinski, A.B., Ronen, A., 2020. Longwave radiative effect of the cloud twilight zone. Nat. Geosci. 13, 669–673. https://doi.org/10.1038/s41561-020-0636-8.

Fabel, Y., Nouri, B., Wilbert, S., Blum, N., Triebel, R., Hasenbalg, M., Kuhn, P., Zarzalejo, L.F., Pitz-Paal, R., 2022. Applying self-supervised learning for semantic cloud segmentation of all-sky images. Atmos. Meas. Tech. 15 (3), 797–809. https://doi.org/10.5194/amt-15-797-2022.

Guest, P.S., 1998. Surface longwave radiation conditions in the eastern Weddell Sea during winter. J. Geophys. Res. Oceans 103 (C13), 30761–30771. https://doi.org/10.1029/98JC02146.

Harrison, L., Michalsky, J., Berndt, J., 1994. Automated multifilter rotating shadow-band radiometer: an instrument for optical depth and radiation measurements. Appl. Opt. 33, 5118–5125. https://opg.optica.org/ao/abstract.cfm?URI=ao-33-22-5118.

Hirsch, E., Koren, I., Levin, Z., Altaratz, O., Agassi, E., 2014. On transition-zone water clouds. Atmos. Chem. Phys. 14 (17), 9001–9012. https://doi.org/10.5194/acp-14-9001-2014.

Jahani, B., Calbó, J., González, J.A., 2019. Transition zone radiative effects in shortwave radiation parameterizations: Case of weather research and forecasting model. J. Geophys. Res. Atmos. 124 (23), 13091–13104. https://doi.org/10.1029/2019JD031064.

Jahani, B., Calbó, J., González, J.A., 2020. Quantifying transition zone radiative effects in longwave radiation parameterizations. Geophys. Res. Lett. 47 (22) https://doi.org/10.1029/2020GL090408.

Jahani, B., Andersen, H., Calbó, J., González, J.A., Cermak, J., 2022. Longwave radiative effect of the cloud–aerosol transition zone based on CERES observations. Atmos. Chem. Phys. 22 (2), 1483–1494. https://doi.org/10.5194/acp-22-1483-2022.

Kazantzidis, A., Tzoumanikas, P., Bais, A.F., Fotopoulos, S., Economou, G., 2012. Cloud detection and classification with the use of whole-sky ground-based images. Atmos. Res. 113, 80–88. https://doi.org/10.1016/j.atmosres.2012.05.005.

Koren, I., Remer, L.A., Kaufman, Y.J., Rudich, Y., Martins, J.V., 2007. On the twilight zone between clouds and aerosols. Geophys. Res. Lett. 34 (8) https://doi.org/10.1029/2007GL029253.

Koren, I., Oreopoulos, L., Feingold, G., Remer, L.A., Altaratz, O., 2008. How small is a small cloud? Atmos. Chem. Phys. 8 (14), 3855–3864. https://doi.org/10.5194/acp-8-3855-2008.

Letu, H., Nagao, T.M., Nakajima, T.Y., Matsumae, Y., 2014. Method for validating cloud mask obtained from satellite measurements using ground-based sky camera. Appl. Opt. 53 (31), 7523–7533. https://doi.org/10.1364/AO.53.007523.

Long, C.N., Ackerman, T.P., 2000. Identification of clear skies from broadband pyranometer measurements and calculation of downwelling shortwave cloud effects. J. Geophys. Res. Atmos. 105 (D12), 15609–15626. https://doi.org/10.1029/2000JD900077.

Long, C.N., Sabburg, J.M., Calbó, J., Pagès, D., 2006a. Retrieving cloud characteristics from ground-based daytime color all-sky images. J. Atmos. Ocean. Technol. 23 (5), 633–652. https://doi.org/10.1175/JTECH1875.1.

Long, C.N., Ackerman, T.P., Gaustad, K.L., Cole, J.N.S., 2006b. Estimation of fractional sky cover from broadband shortwave radiometer measurements. J. Geophys. Res. Atmos. 111 (D11) https://doi.org/10.1029/2005JD006475.

Lu, M.L., Wang, J., Freedman, A., Jonsson, H.H., Flagan, R.C., McClatchey, R.A., Seinfeld, J.H., 2003. Analysis of humidity halos around trade wind cumulus clouds. J. Atmos. Sci. 60 (8), 1041–1059. https://doi.org/10.1175/1520-0469(2003)60<1041:AOHHAT>2.0.CO;2.

Marty, C., Philipona, R., 2000. The clear-sky index to separate clear-sky from cloudy-sky situations in climate research. Geophys. Res. Lett. 27 (17), 2649–2652. https://doi.org/10.1029/2000GL011743.

Ohmura, A., 1982. Climate and energy balance on the Arctic tundra. J. Climatol. 2 (1), 65–84. https://doi.org/10.1002/joc.3370020106.

Perry, K.D., Hobbs, P.V., 1996. Influences of isolated cumulus clouds on the humidity of their surroundings. J. Atmos. Sci. 53 (1), 159–174. https://doi.org/10.1175/1520-0469(1996)053<0159:IOICCO>2.0.CO;2.

Román, R., Antuña-Sánchez, J.C., Cachorro, V.E., Toledano, C., Torres, B., Mateos, D., Fuertes, D., López, C., González, R., Lapionok, T., Herreras-Giralda, M., Dubovik, O., de Frutos, Á.M., 2022. Retrieval of aerosol properties using relative radiance measurements from an all-sky camera. Atmos. Meas. Tech. 15 (2), 407–433. https://doi.org/10.5194/amt-15-407-2022.

Schwartz, S.E., Huang, D., Vladutescu, D.V., 2017. High-resolution photography of clouds from the surface: Retrieval of optical depth of thin clouds down to centimeter scales. J. Geophys. Res. Atmos. 122 (5), 2898–2928. https://doi.org/10.1002/2016JD025384.

Schwarz, K., Cermak, J., Fuchs, J., Andersen, H., 2017. Mapping the twilight zone—what we are missing between clouds and aerosols. Remote Sens. 9 (6), 577. https://doi.org/10.3390/rs9060577.

Sohn, B.J., Nakajima, T., Satoh, M., Jang, H.S., 2010. Impact of different definitions of clear-sky flux on the determination of longwave cloud radiative forcing: NICAM simulation results. Atmos. Chem. Phys. 10, 11641–11646. https://doi.org/10.5194/acp-10-11641-2010.

Spänkuch, D., Hellmuth, O., Görsdorf, U., 2022. What is a cloud? Toward a more precise definition? B. Am. Meteorol. Soc. 103 (8), E1894–E1929. https://doi.org/10.1175/BAMS-D-21-0032.1.

Tapakis, R., Charalambides, A.G., 2013. Equipment and methodologies for cloud detection and classification: a review. Sol. Energy 95, 392–430. https://doi.org/10.1016/j.solener.2012.11.015.

Várnai, T., Marshak, A., 2009. MODIS observations of enhanced clear sky reflectance near clouds. Geophys. Res. Lett. 36 (6) https://doi.org/10.1029/2008GL037089.

Viúdez-Mora, A., Calbó, J., González, J.A., Jiménez, M.A., 2009. Modeling atmospheric longwave radiation at the surface under cloudless skies. J. Geophys. Res. Atmos. 114 (D18) https://doi.org/10.1029/2009JD011885.

Viúdez-Mora, A., Costa-Surós, M., Calbó, J., González, J.A., 2015. Modeling atmospheric longwave radiation at the surface during overcast skies: the role of cloud base height. J. Geophys. Res. Atmos. 120 (1), 199–214. https://doi.org/10.1002/2014JD022310.

Yang, W., Marshak, A., McBridec, P.J., Chiu, J.C., Knyazikhine, Y., Schmidt, K.S., Flynn, C., Lewish, E.R., Eloranta, E.W., 2016. Observation of the spectrally invariant properties of clouds in cloudy-to-clear transition zones during the MAGIC field campaign. Atmos. Res. 182, 294–301. https://doi.org/10.1016/j.atmosres.2016.08.004.